Electronic Supplementary Material (ESI) for New Journal of Chemistry.

Supplementary Information

Nitration of Benzothioxanthene: a new step towards functionalization of the core

José María Andrés Castán,[†+] Laura Abad Galán,[≠+] Shi Li,[‡] Clément Dalinot,[†] Pablo Simón Marqués,[†] Magali Allain,[†] Chad Risko,[‡*] Cyrille Monnereau,[≠] Olivier Maury,[≠*] Philippe Blanchard,[†] Clément Cabanetos[†*].

†Laboratoire MOLTECH-Anjou, UMR CNRS 6200, UNIV Angers, SFR MATRIX, 2 Bd Lavoisier, 49045 Angers Cedex, France

‡Department of Chemistry & Center for Applied Energy Research, University of Kentucky, Lexington, KY 40506, USA

≠ Univ Lyon, ENS de Lyon, CNRS UMR 5182, Université Claude Bernard Lyon 1, F-69342 Lyon, France.

Table of contents

NMR spectra

^{1}H NMR (CDCl$_3$, 500 MHz)

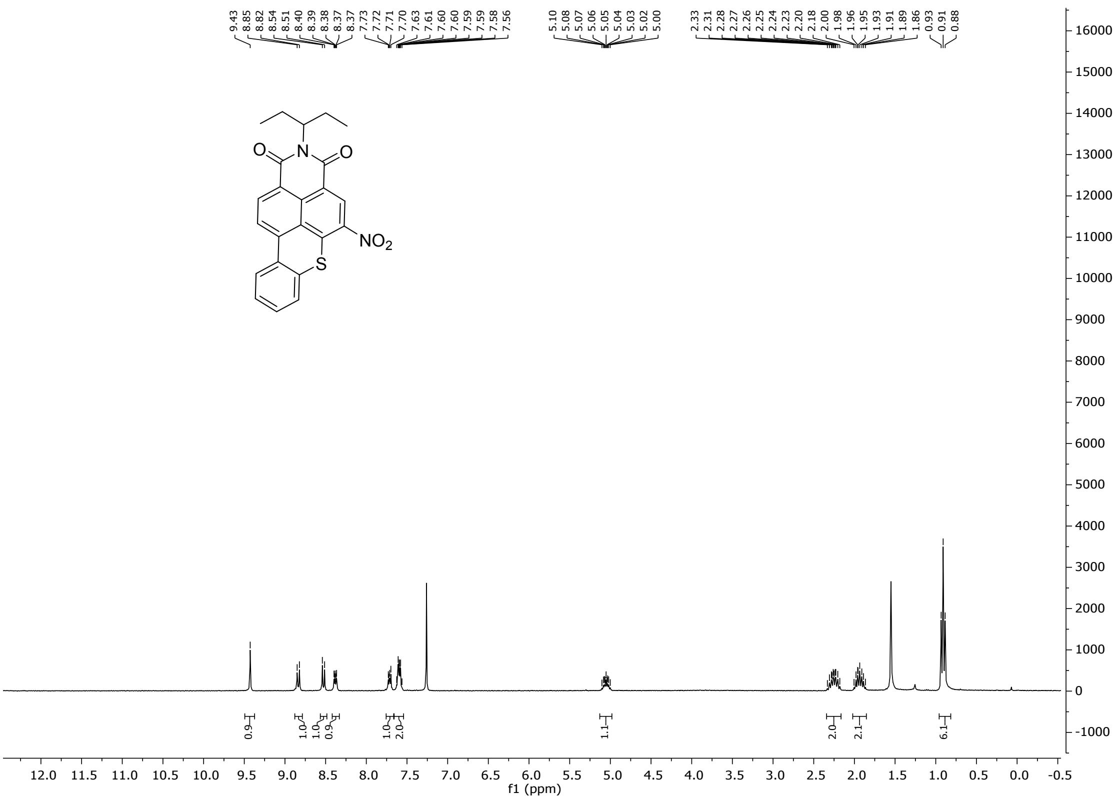

^{13}C NMR (CDCl$_3$, 125 MHz)

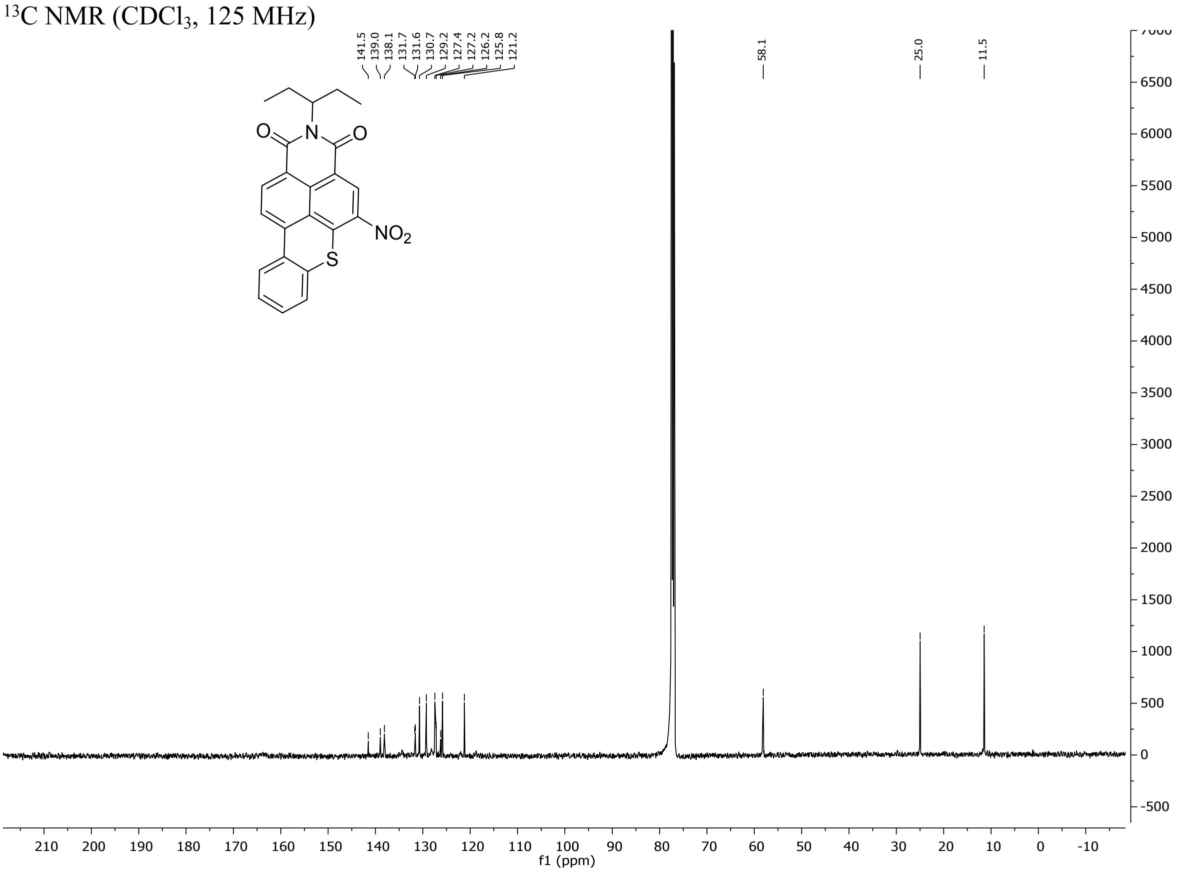

^{1}H NMR (CDCl$_3$, 300 MHz)

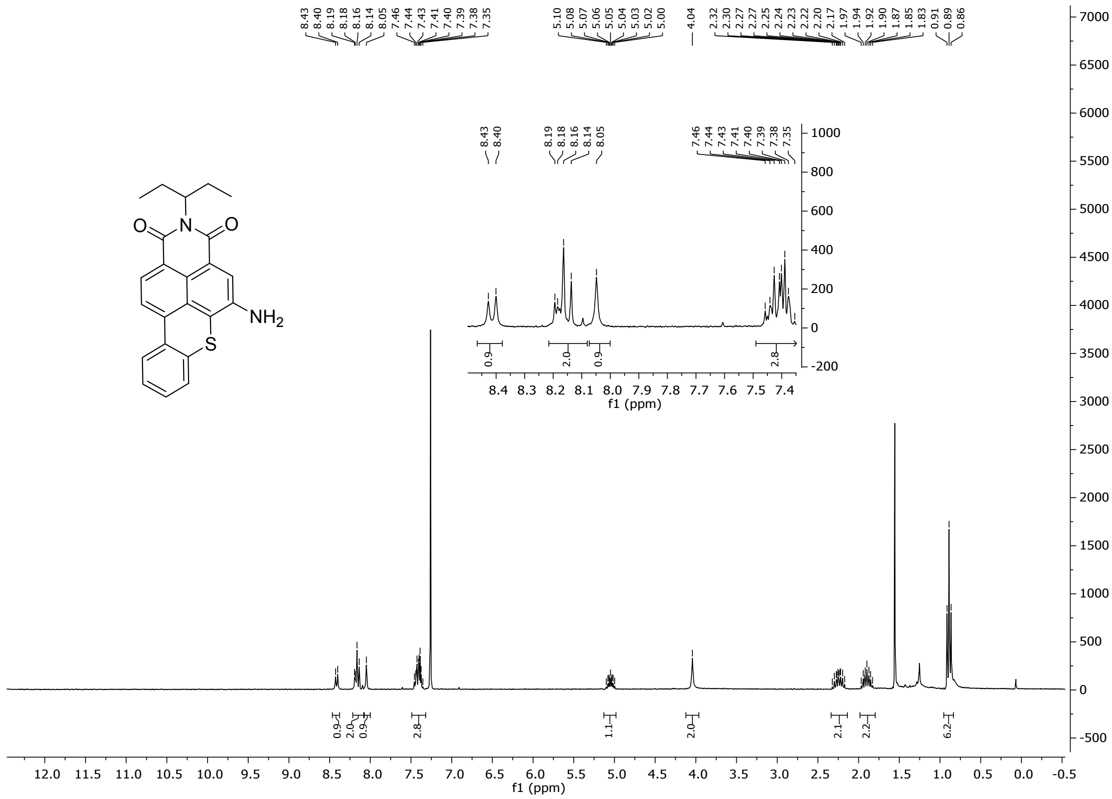

^{13}C NMR (CDCl$_3$, 125 MHz)

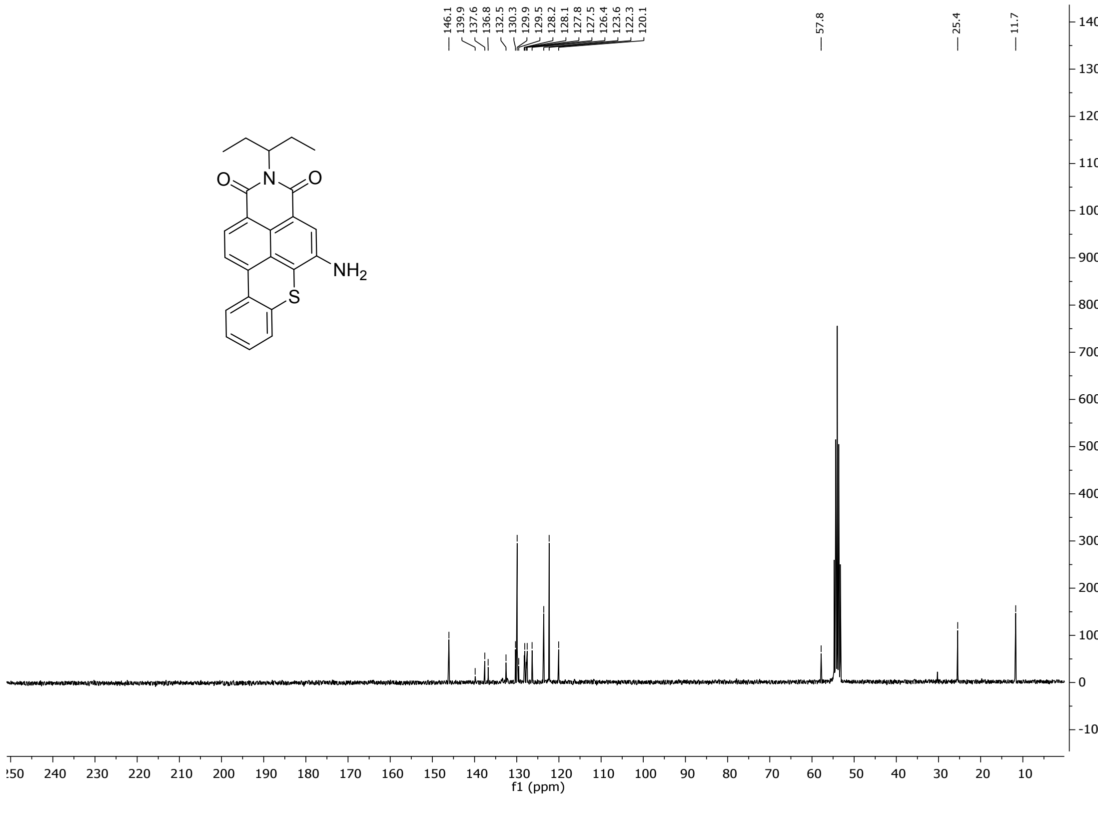

^1H NMR (CD_2Cl_2, 300 MHz)

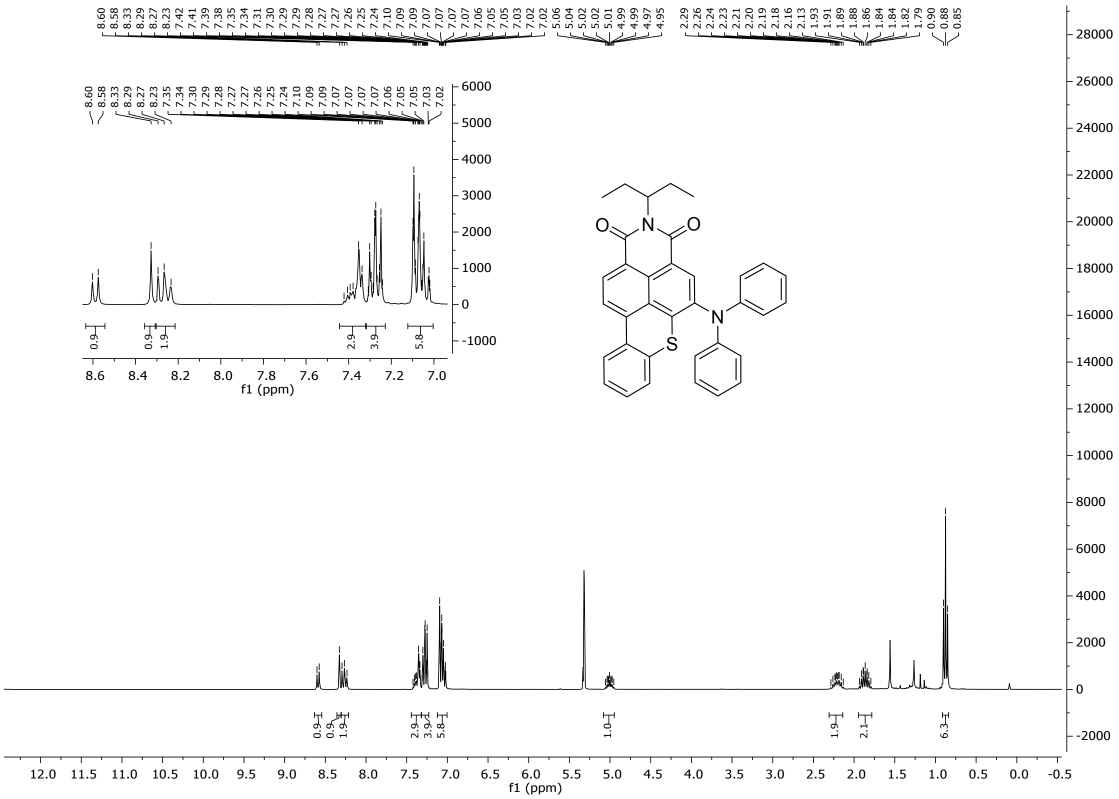

^{13}C NMR (CD_2Cl_2, 75 MHz)

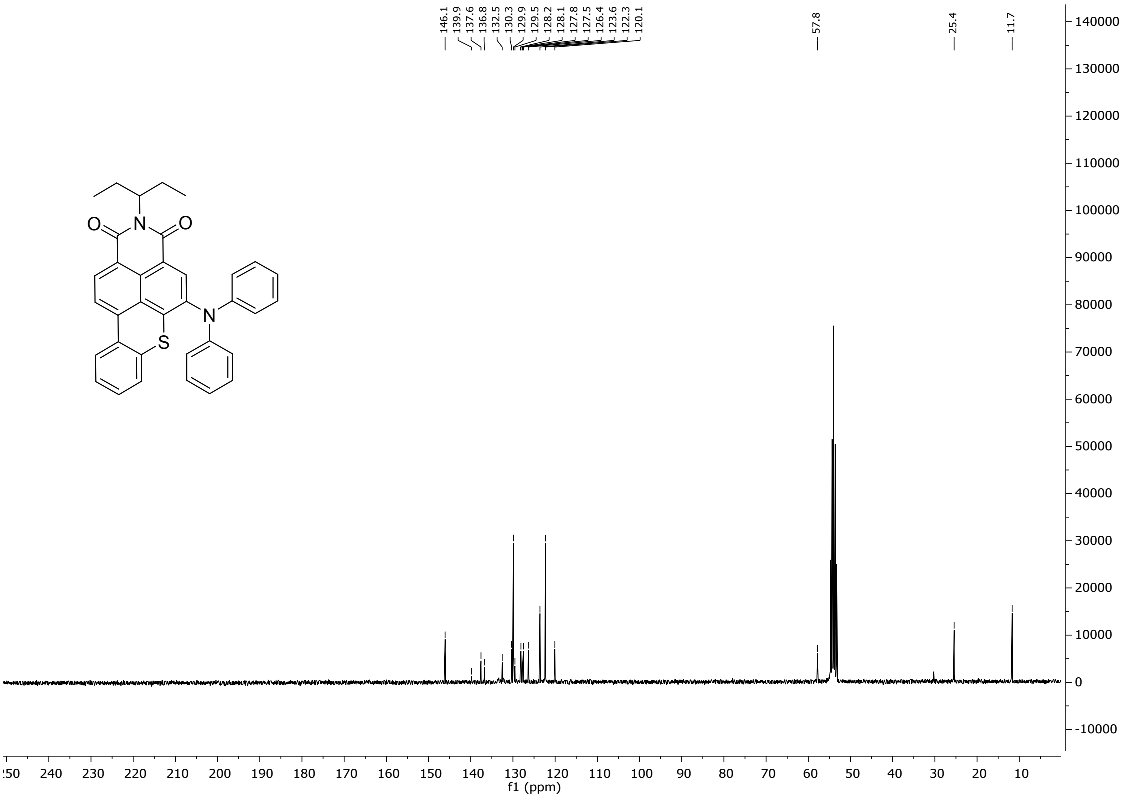

^{1}H NMR (CDCl$_3$, 300 MHz)

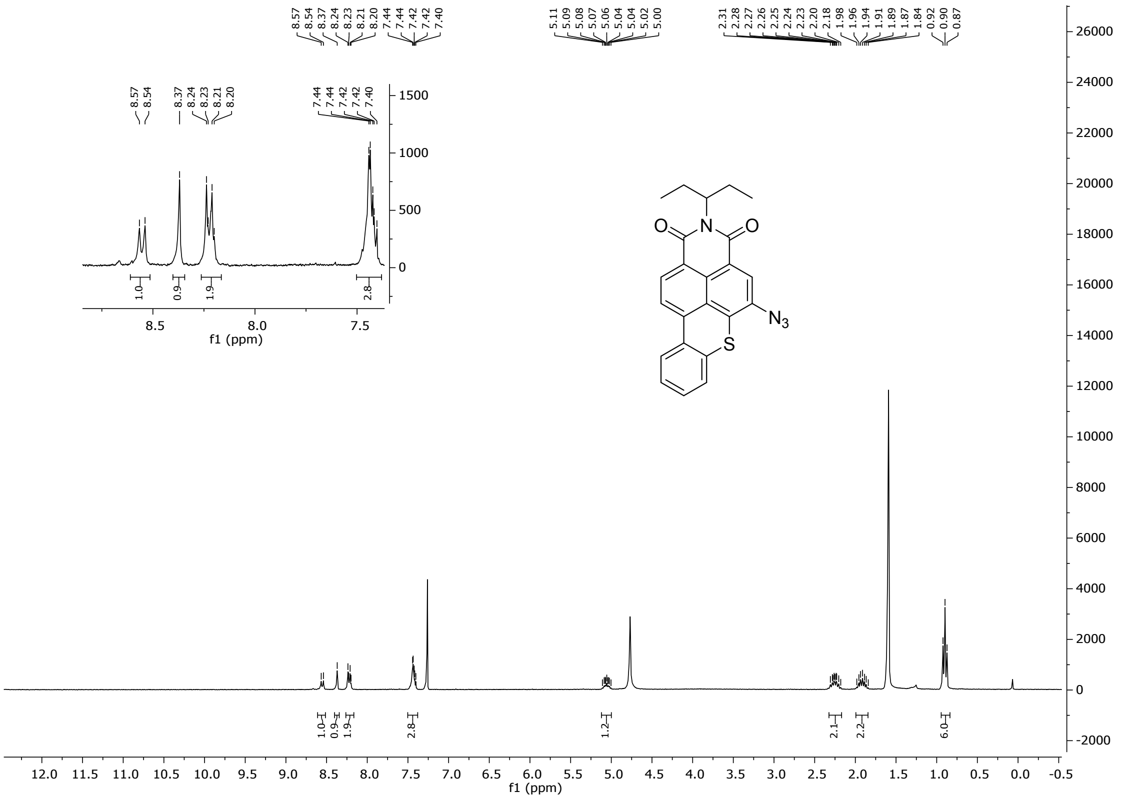

^{13}C NMR: Due to stability issues, we were unable to obtain a complete ^{13}C NMR spectrum.

^1H NMR ($CDCl_3$, 300 MHz)

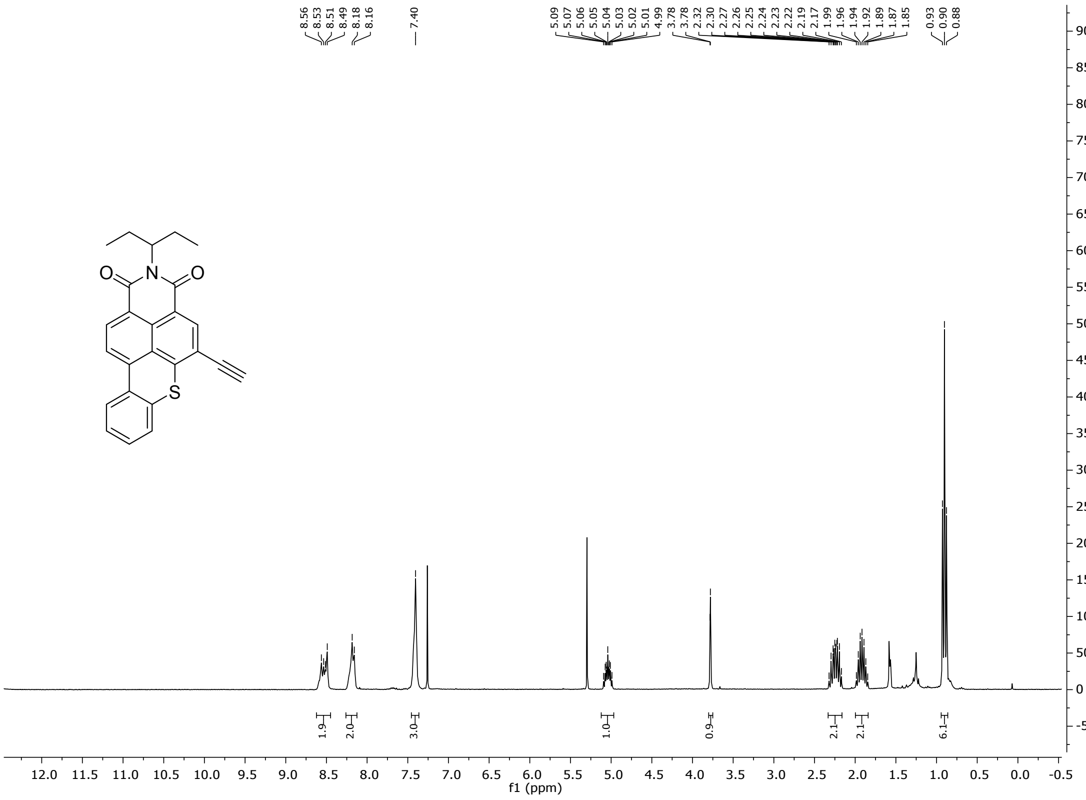

^{13}C NMR ($CDCl_3$, 75 MHz)

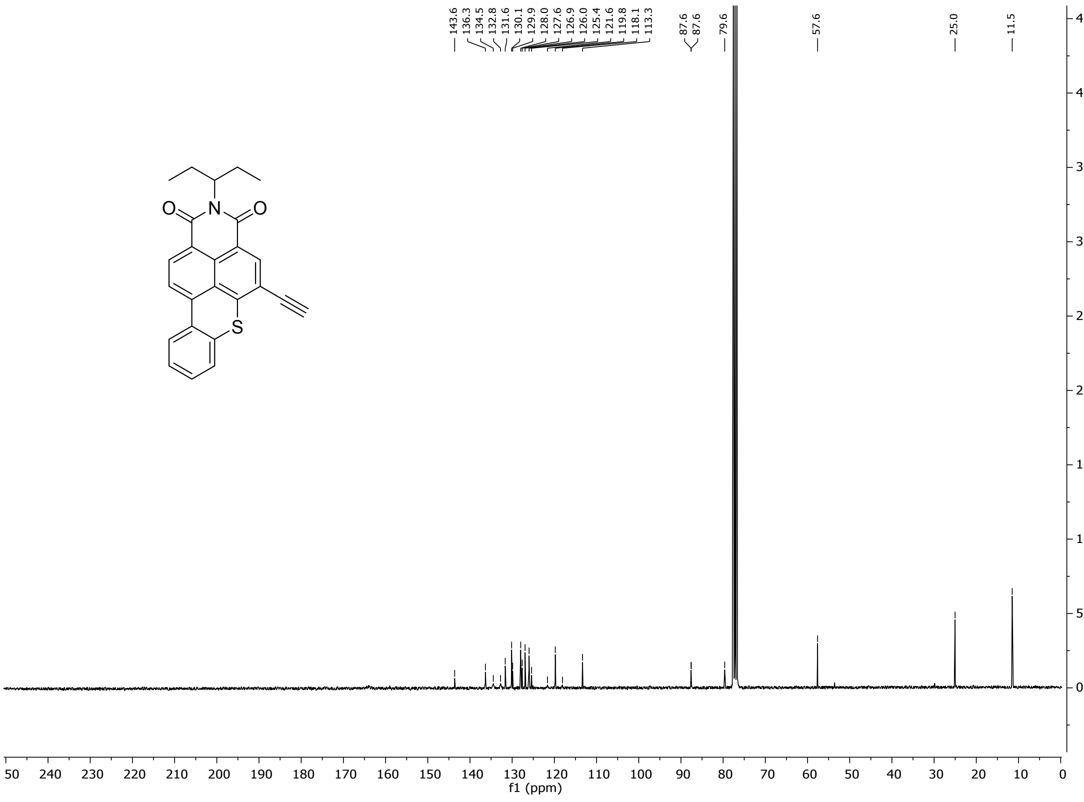

^{1}H NMR (CDCl$_3$, 300 MHz)

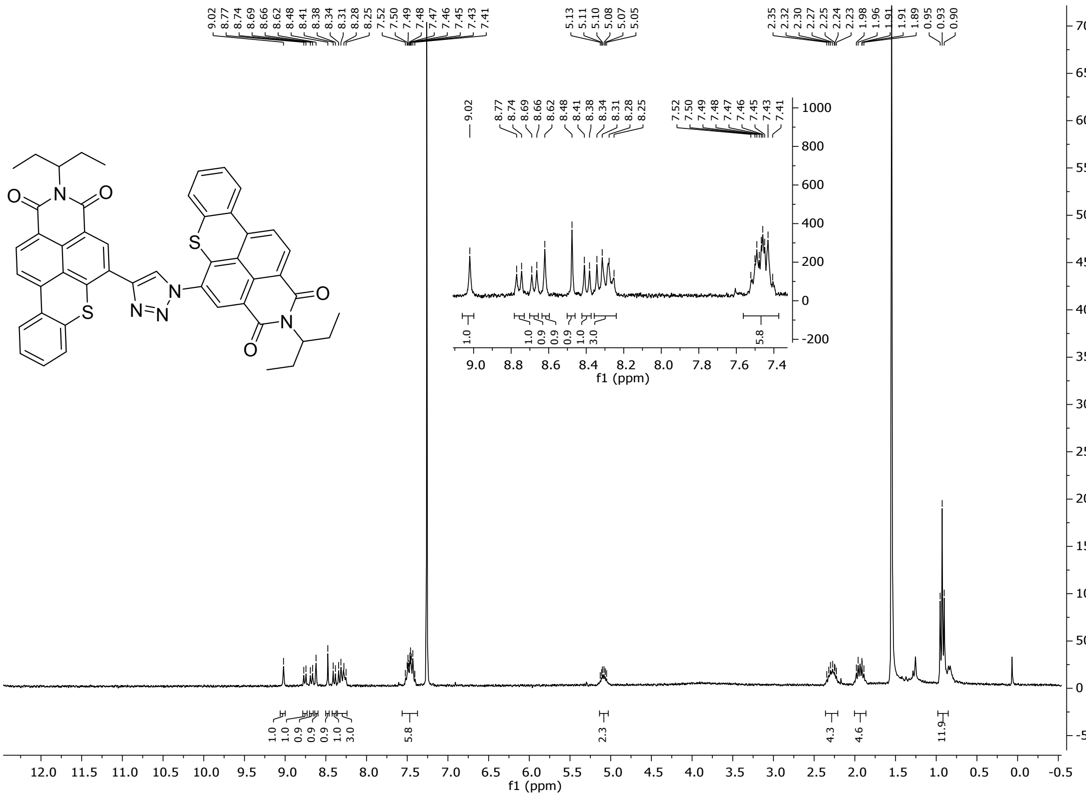

^{13}C NMR (CDCl$_3$, 125 MHz)

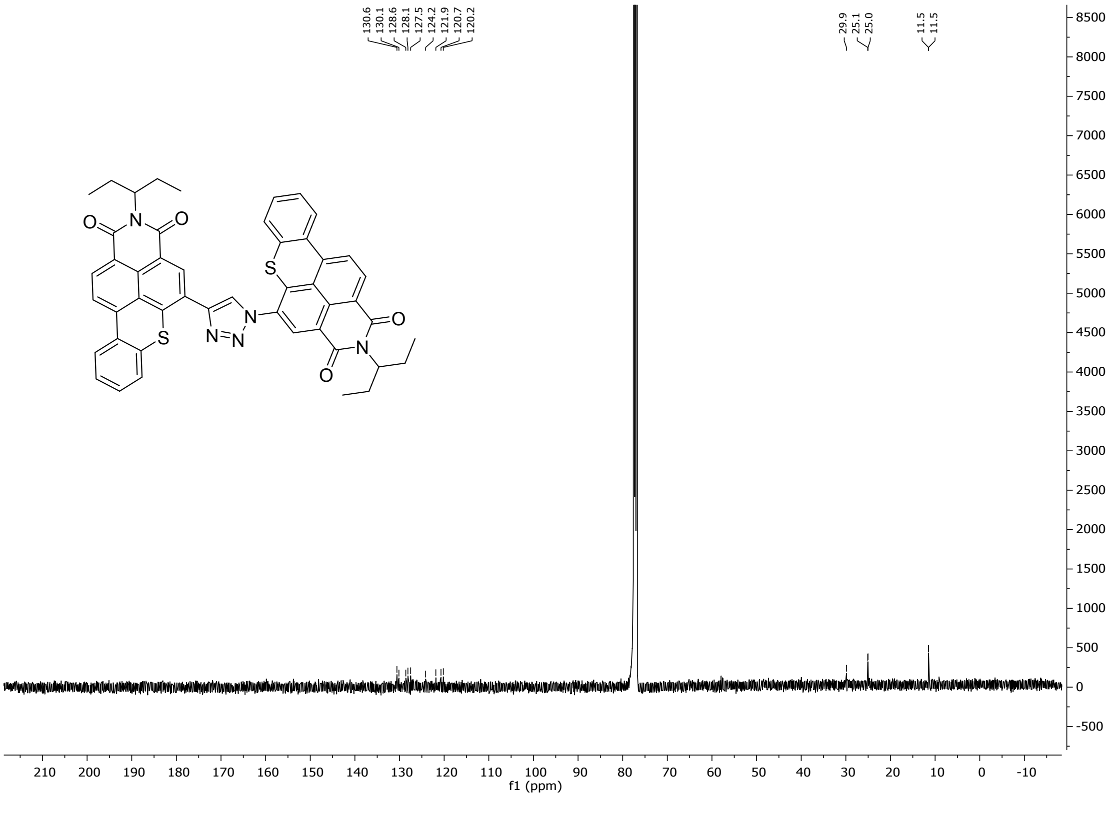

Mass spectra

HRMS (EI): *m/z* calcd for $C_{23}H_{18}N_2O_4S$: 418.0982, found: 418.0986 (Δ = 1.0 ppm).

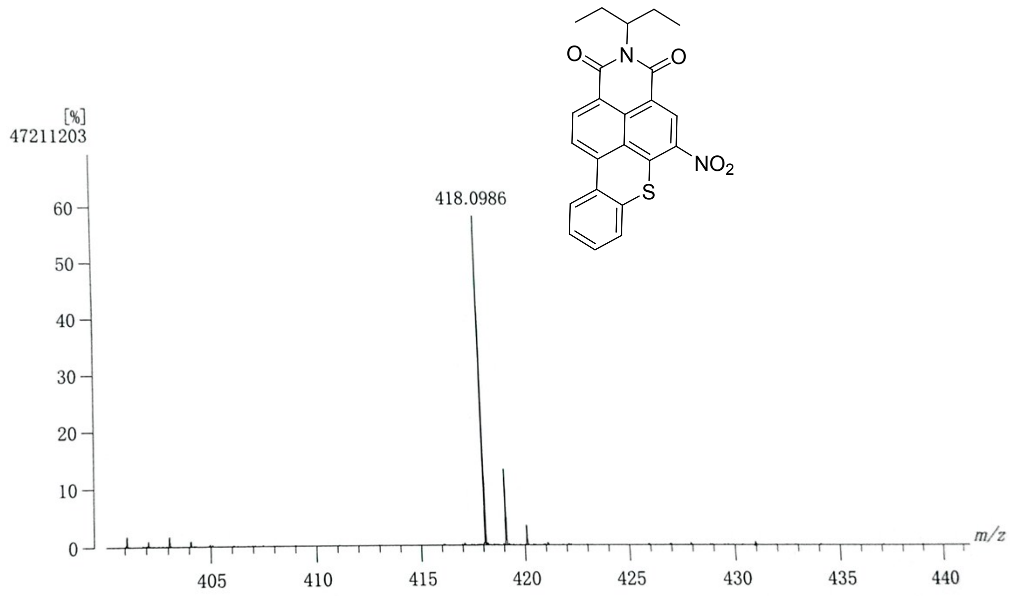

HRMS (FAB): *m/z* calcd for $C_{23}H_{20}N_2O_2S$: 388.1240, found: 388.1250 (Δ = 2.6 ppm).

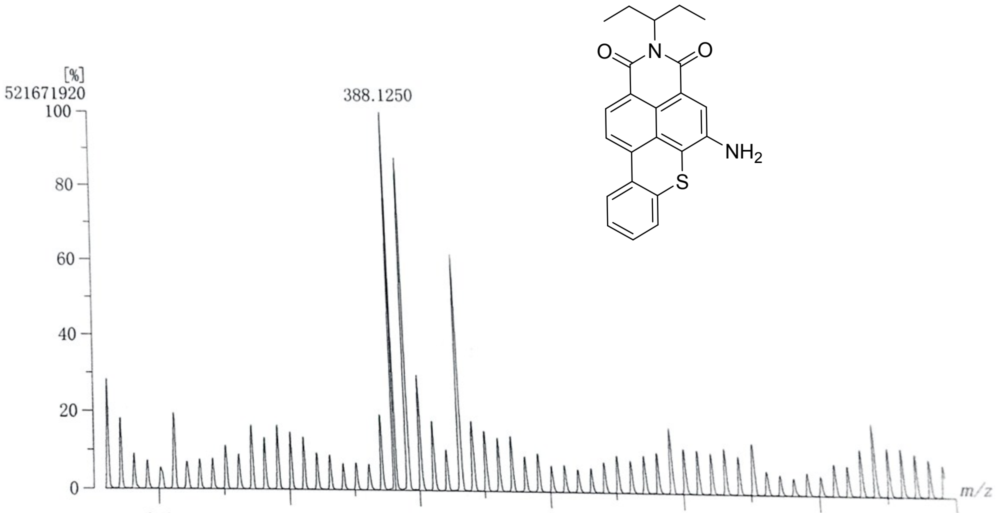

HRMS (EI): *m/z* calcd for $C_{35}H_{28}N_2O_2S$: 540.1866, found: 540.1864 (Δ = 0.4 ppm).

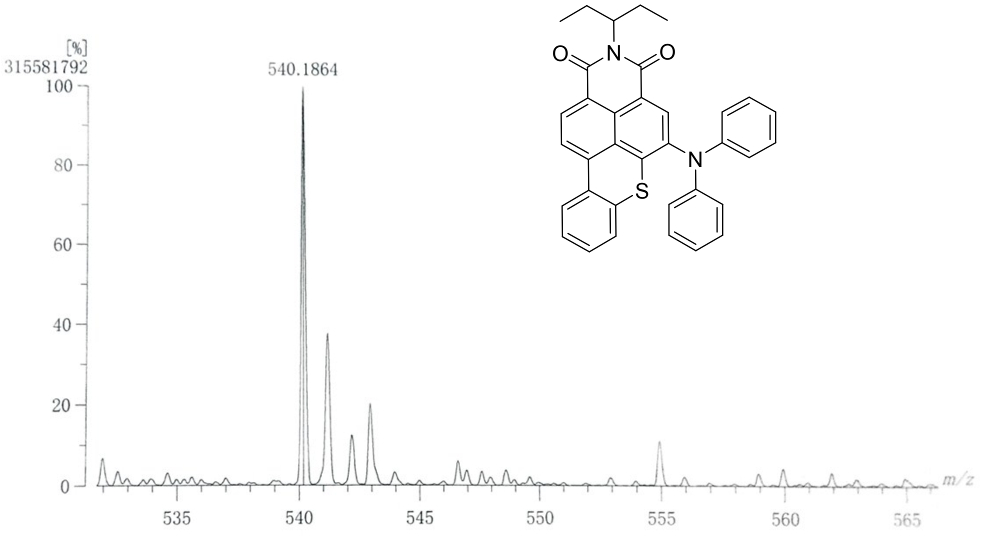

MS (MALDI): *m/z* calcd for $C_{23}H_{18}N_4O_2S$: 414.48, found: 305 $[M\text{-}H\text{-}N_2]^+$. Due to stability issues during the measurements, we were unable to obtain the HRMS spectrum.

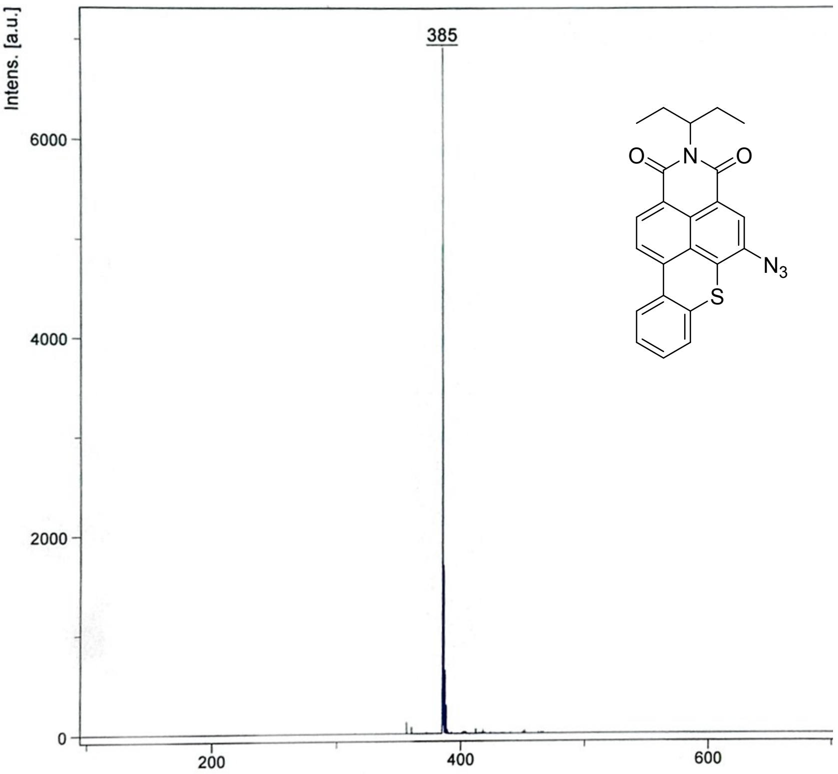

HRMS (FAB): *m/z* calcd for $C_{25}H_{19}NO_2S$: 397.1131, found: 397.1136 (Δ = 1.3 ppm).

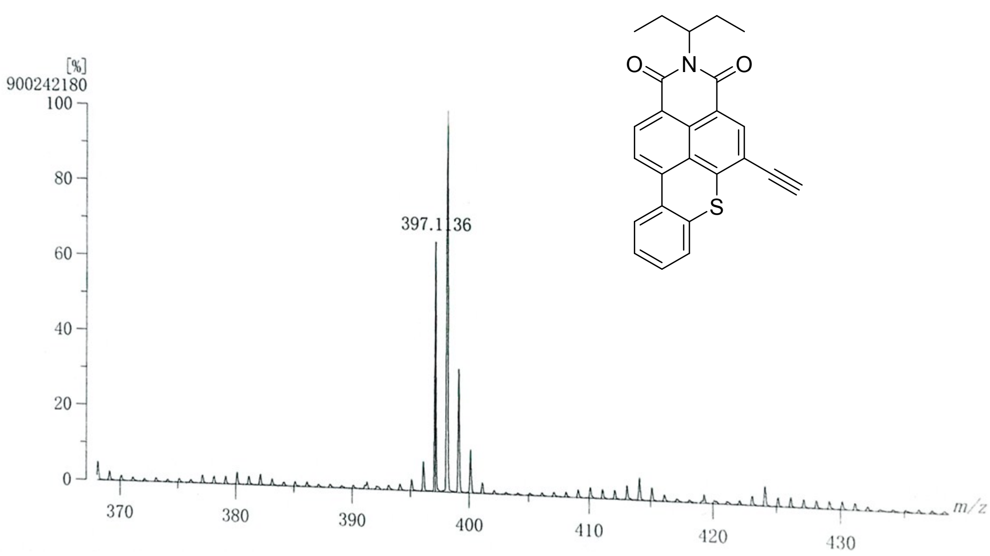

HRMS (FAB): *m/z* calcd for $C_{48}H_{38}N_5O_4S_2$: 812.2360, found: 812.2364 $[M+H]^+$ (Δ = 0.5 ppm).

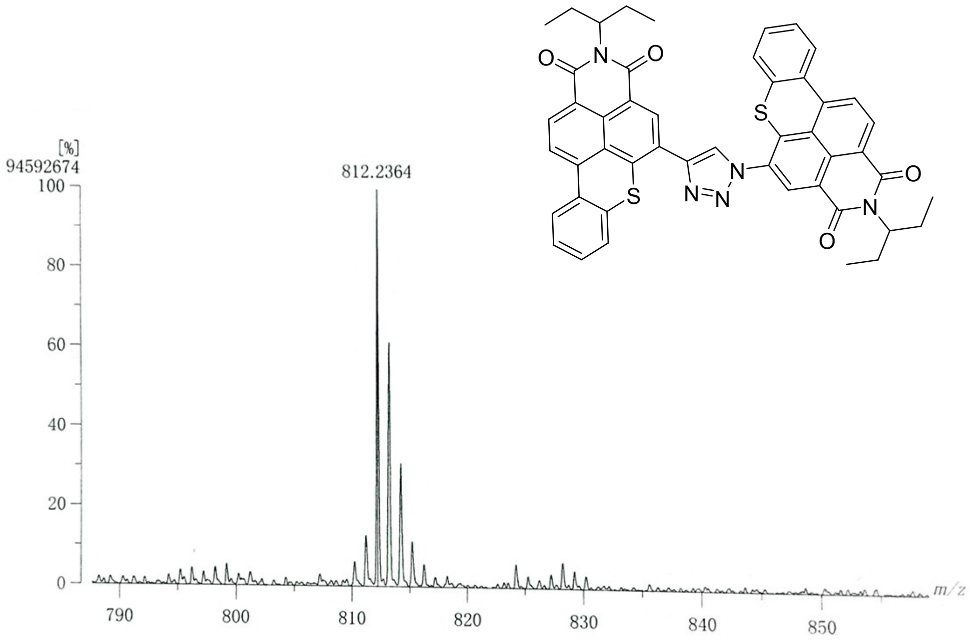

Supporting figures

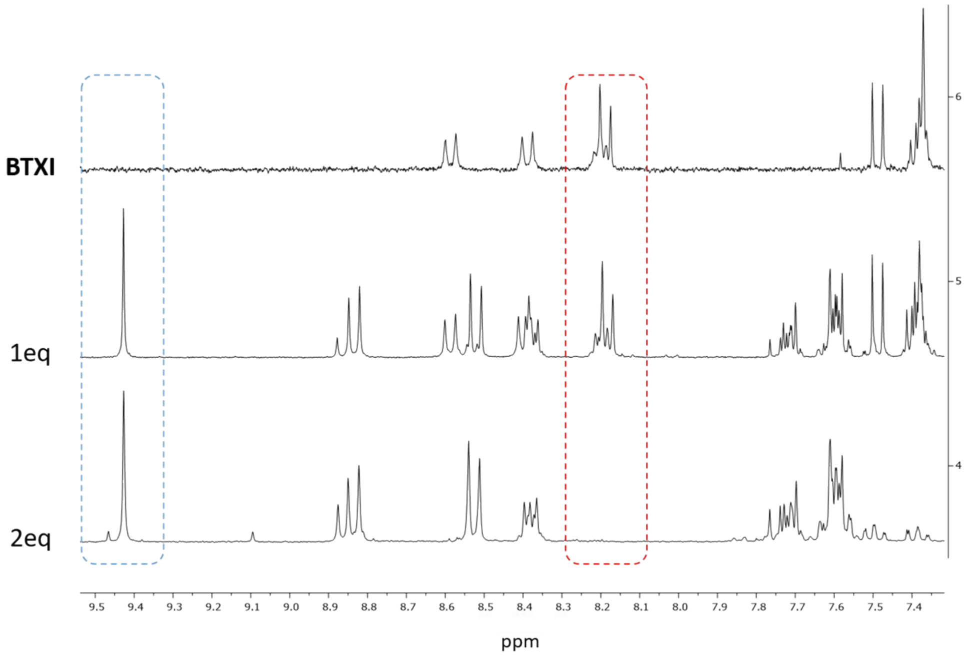

Figure S1-A. ^{1}H-NMR (300 MHz, $CDCl_3$) spectra of the reaction mixtures depending on the number of molar equivalent of nitric acid added to **BTXI** at room temperature.

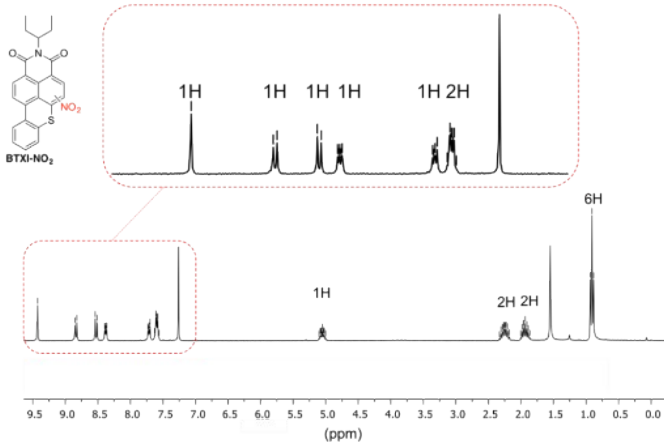

Figure S1-B. ^{1}H-NMR (300 MHz, $CDCl_3$) of the mono nitrated BTXI derivative (**BTXI-NO$_2$**).

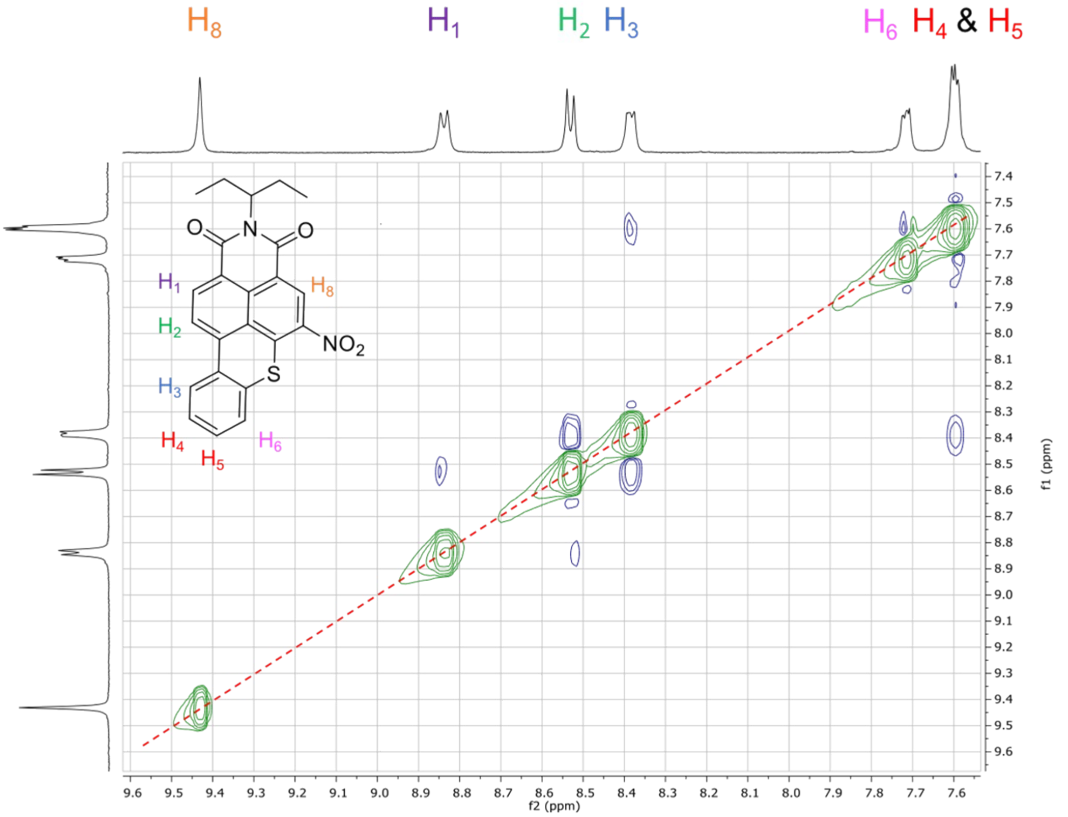

Figure S2. 2D NOESY spectrum of **BTXI-NO$_2$** recorded in deuterated chloroform at room temperature.

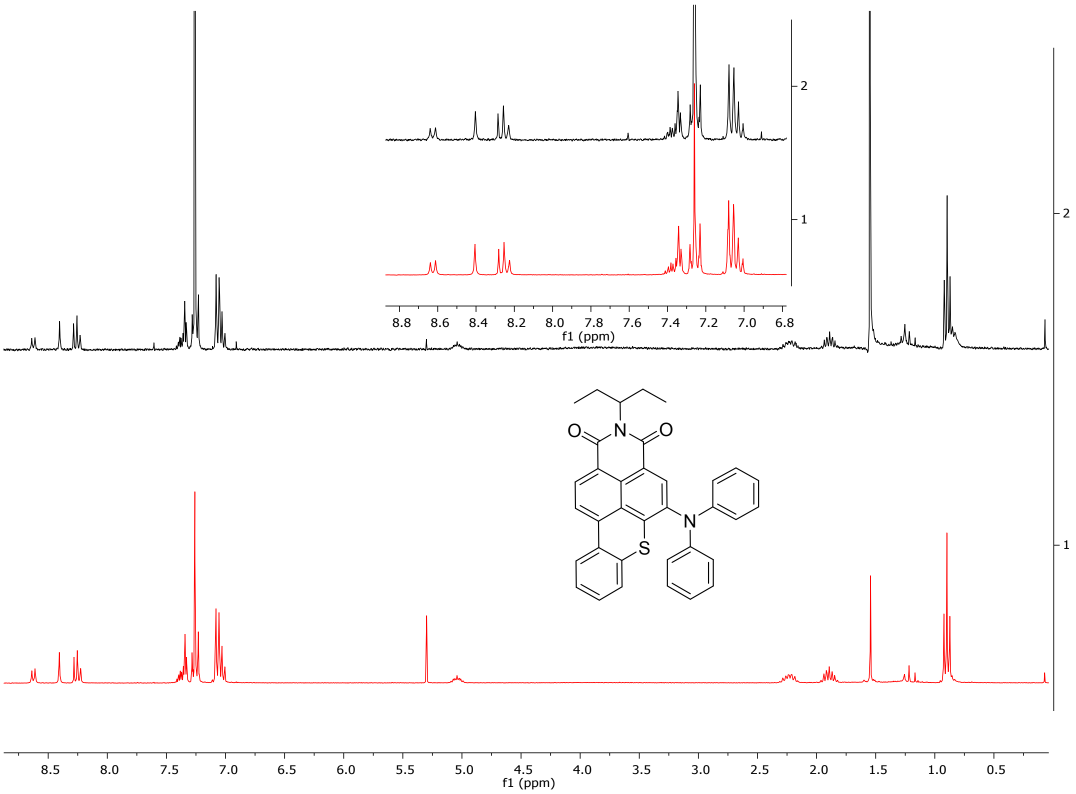

Figure S3. Direct comparison of (A)-**BTXI-NPh$_2$** (black) and (B)-**BTXI-NPh$_2$** ^{1}H NMR spectra (red) recorded in deuterated chloroform at room temperature.

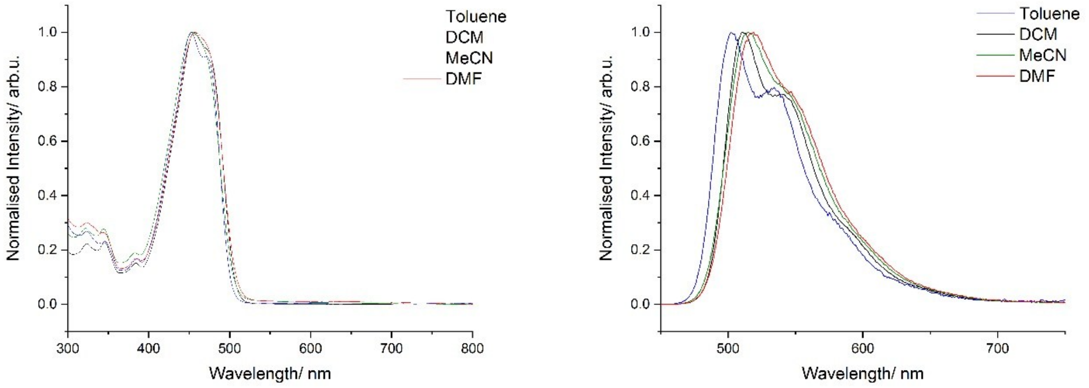

Figure S4. Normalized absorption (left) and emission (right) in toluene (blue trace), dichloromethane (black trace), acetonitrile (green trace) and *N*-*N*-dimethylformamide (red trace) at room temperature of **BTXI**.

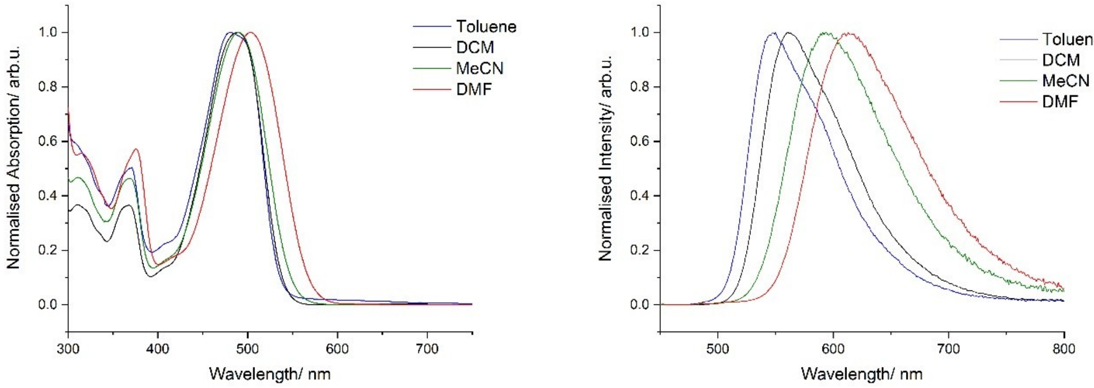

Figure S5. Normalized absorption and emission in toluene (blue trace), dichloromethane (black trace), acetonitrile (green trace) and *N*-*N*-dimethylformamide (red trace) at room temperature of **BTXI-NH$_2$**.

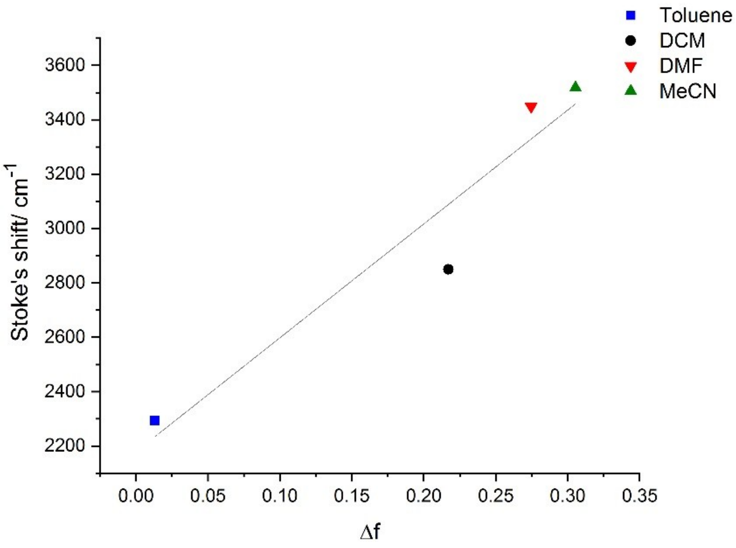

Figure S6. Stokes shift of **BTXI-NH$_2$** following the Lippert-Mataga equation.

The relationship between Stokes shift and the polarizability of solvent can be described following the Lippert–Mataga equation:

$$\Delta \nu = \frac{2\Delta f}{4\pi\varepsilon_0 \mathrm{h} c a^3}(\mu_e - \mu_g)^2 + b$$

$$\Delta f = \frac{\varepsilon - 1}{2\varepsilon + 1} - \frac{n^2 - 1}{2n^2 + 1}$$

where Δv is the Stokes shift, h is the Planck constant, c is the light speed, a is the Onsager cavity radius, and μe, μg are the excited and ground-state dipole moments, respectively. Δf, is known as the solvent polarizability and can be calculated using the dielectric constants (ε) and refractive indices (n).

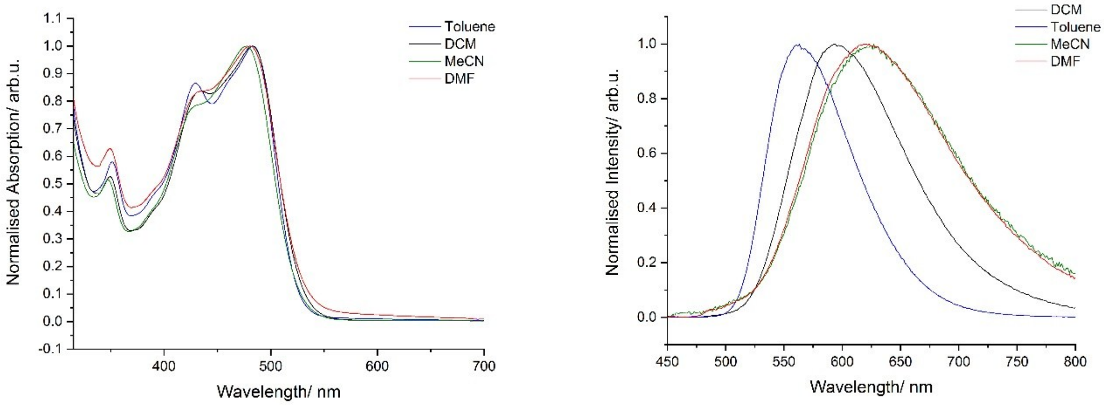

Figure S7. Normalized absorption (left) and emission (right) in toluene (blue trace), dichloromethane (black trace), acetonitrile (green trace) and *N*-*N*-dimethylformamide (red trace) at room temperature of **BTXI-NPh$_2$**.

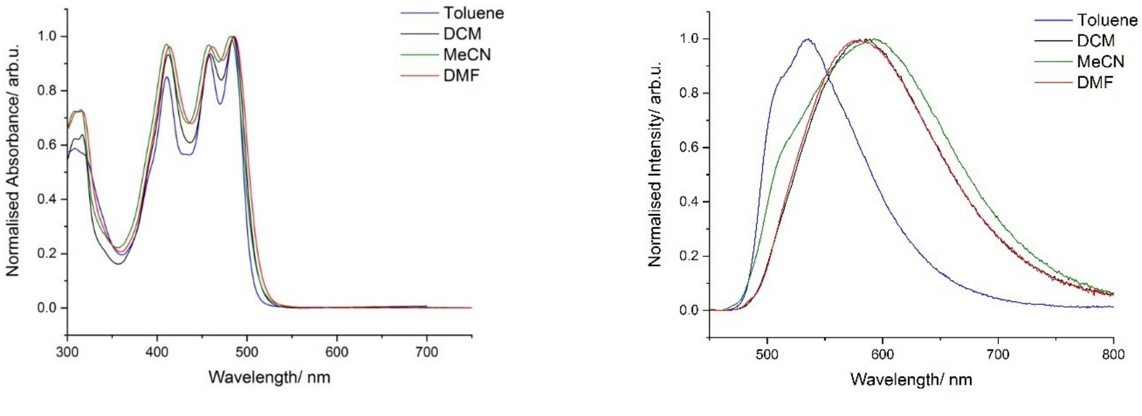

Figure S8. Normalized absorption (left) and emission (right) in toluene (blue trace), dichloromethane (black trace), acetonitrile (green trace) and *N*-*N*-dimethylformamide (red trace) at room temperature of **BTXI-NO$_2$**.

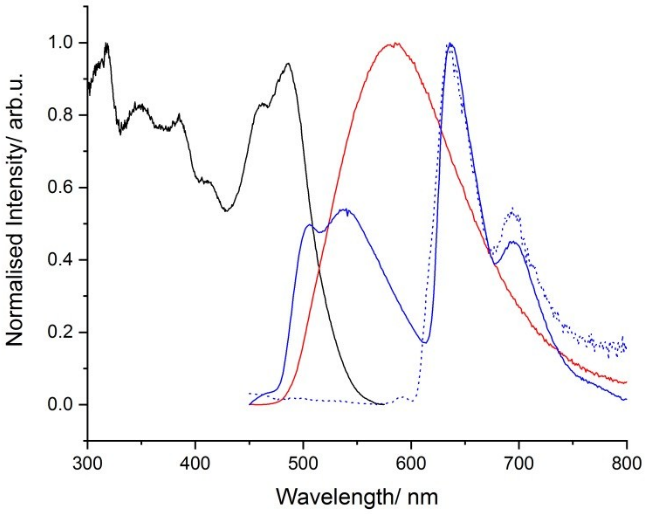

Figure S9. Normalized excitation (λ_{em}= 585 nm) (black trace), emission (λ_{exc}= 425 nm) at room temperature (red trace) and at 77K in a mixture MeOH:EtOH (1:4) without (blue solid trace) and with a 0.05 ms delay (blue dotted trace) of **BTXI-NO$_2$**.

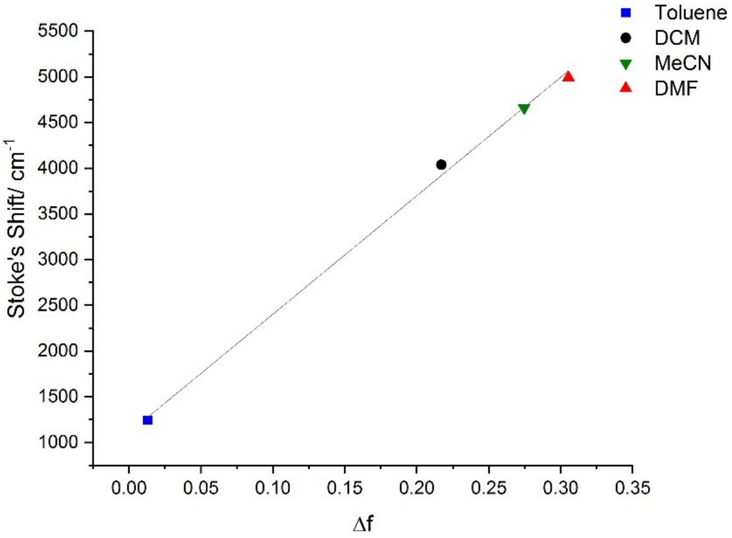

Figure S10. Stokes shift **BTXI-NPh$_2$** versus solvent polarizability following the Lippert-Mataga equation.

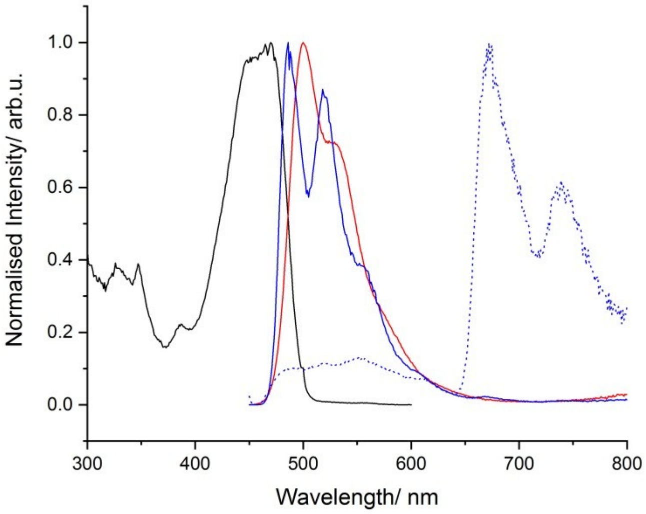

Figure S11. Normalized excitation (λ_{em}= 585 nm) (black trace), emission (λ_{exc}= 425 nm) at room temperature (red trace) and at 77K in a mixture MeOH:EtOH (1:4) without (blue solid trace) and with a 0.05 ms delay (blue dotted trace) of **BTXI-Br**.

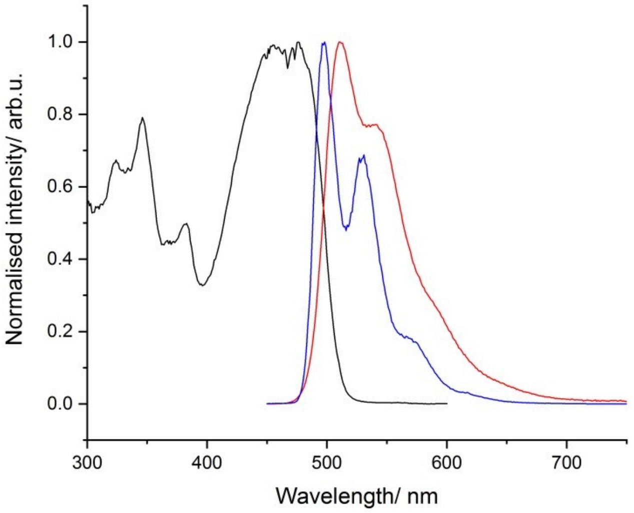

Figure S12. Normalized excitation (λ_{em}= 510 nm) (black trace), emission (λ_{exc}= 425 nm) at room temperature (red trace) and at 77K in a mixture MeOH:EtOH (1:4) (blue trace) of **BTXI**.

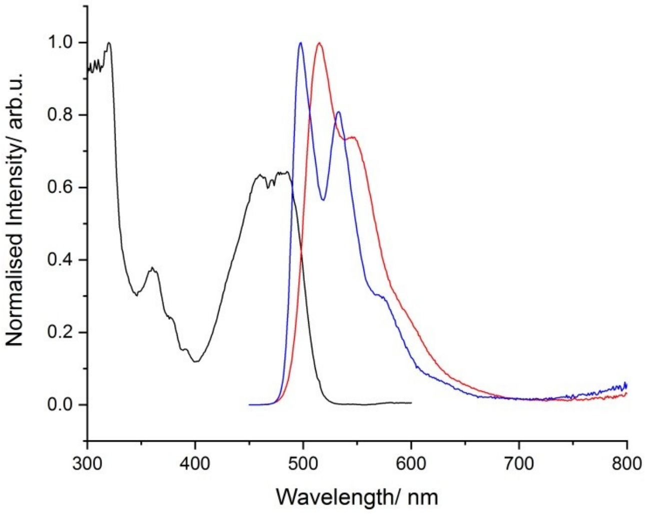

Figure S13. Normalized excitation (λ_{em}= 530 nm) (black trace) and emission (λ_{exc}= 425 nm) at room temperature (red trace) and 77K in a mixture MeOH:EtOH (1:4) (blue trace) of **BTXI-TMS**.

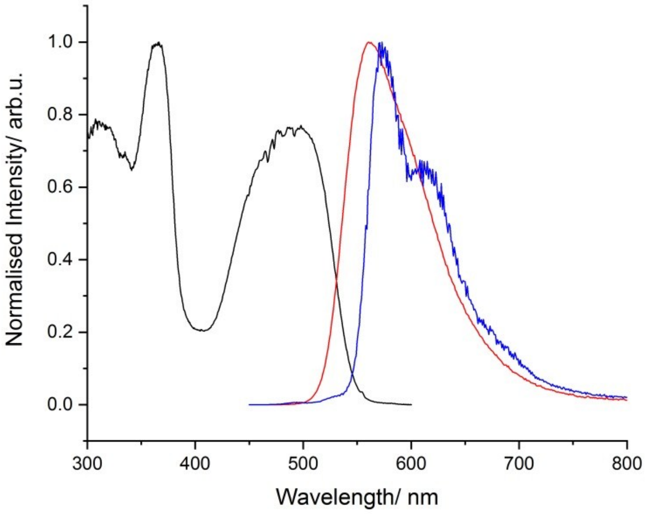

Figure S14. Normalized excitation (λ_{em}= 555 nm) (black trace), emission (λ_{exc}= 425 nm) at room temperature (red trace) and 77K in a mixture MeOH:EtOH (1:4) (blue trace) of **BTXI-NH$_2$**.

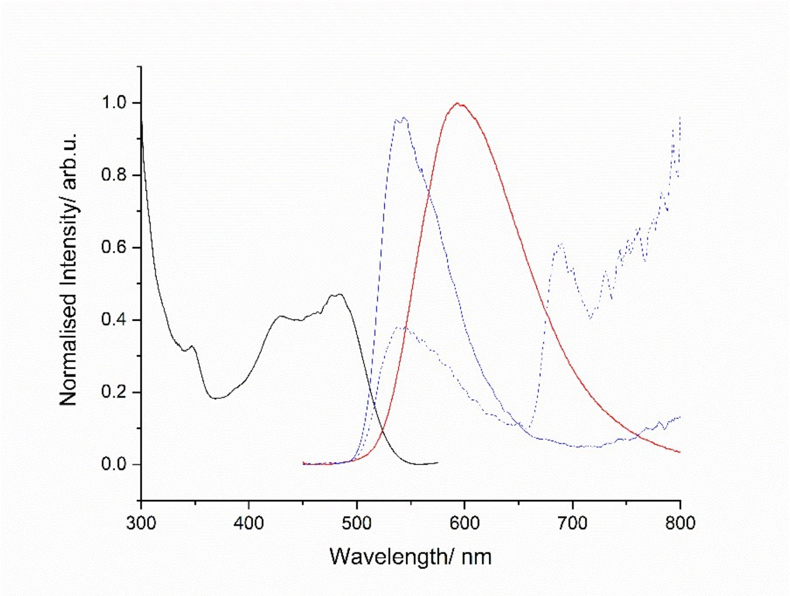

Figure S15. Normalized excitation (λ_{em}= 5600 nm) (black trace), emission (λ_{exc}= 425 nm) at room temperature (red trace) and 77K in a mixture MeOH:EtOH (1:4) without (blue solid trace) and with a 0.05 ms delay (blue dotted trace) of **BTXI-NPh$_2$**.

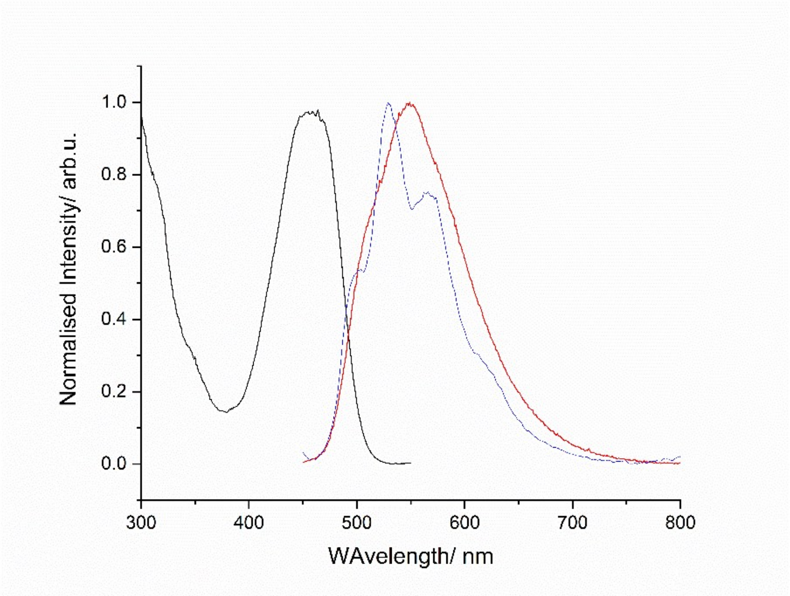

Figure S16. Normalized excitation (λ_{em}= 555 nm) (black trace), emission (λ_{exc}= 425 nm) at room temperature (red trace) and 77K in a mixture MeOH:EtOH (1:4) (blue trace) of **BTXI-N$_3$**.

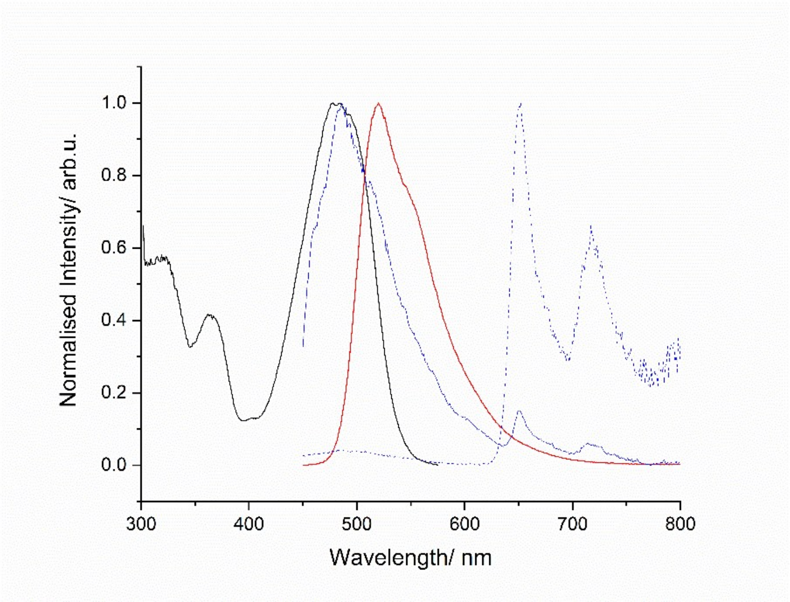

Figure S17. Normalized excitation (λ_{em}= 520 nm) (black trace), emission (λ_{exc}= 425 nm) at room temperature (red trace) and 77K in a mixture MeOH:EtOH (1:4) without (blue solid trace) and with a 0.05 ms delay (blue dotted trace) of **BTXI-Tr-BTXI**.

Density Functional Theory (DFT) Calculations

All density functional theory (DFT) and time-dependent DFT (TDDFT) calculations were carried out at the OT-ωB97X-D/6-31g(d,p) level of theory, with the tuned ω parameter reported in Table S1. The gap-tuned optimized ω parameter for corresponding compound was used for all subsequent calculations. All optimized, unconstrained geometries were confirmed as minima on the potential energy surface through normal mode analyses. Note that all alkyl groups were truncated to methyl groups to reduce the computational cost. The Gaussian 16 (Revision A.03) software suite was used for all DFT and TDDFT calculations.

Table S1. Select DFT and TDDFT data for **BTXI** derivatives as determined at the TD-OT-ωB97X-D/6-31g(d,p) level of theory.

	Tuned ω	**IP (eV)**	**EA (eV)**	**S_0-S_1 (eV [nm])**	***f***	**Electronic configuration**
BTXI	0.1728	7.14	1.14	3.28 [378]	0.4313	HOMO → LUMO (97%)
BTXI-Br	0.1648	7.21	1.28	3.25 [382]	0.3974	HOMO → LUMO (97%)
BTXI-NO_2	0.1661	7.57	1.61	3.23 [384]	0.3386	HOMO → LUMO (95%)
BTXI-NH_2	0.1697	6.70	1.04	3.06 [405]	0.3116	HOMO → LUMO (97%)
BTXI-NPh_2	0.1379	6.44	1.20	2.90 [428]	0.1725	HOMO → LUMO (95%)
BTXI-N_3	0.1625	7.00	1.29	3.12 [398]	0.3794	HOMO → LUMO (97%)
BTXI-Tr-BTXI	0.1455	6.76	1.57	3.12 [398]	0.3373	HOMO → LUMO + 1 (95%)

Table S2. Change of enthalpy and Gibbs free energies of the reactions to form **BTXI-NO$_2$**.

	ΔH (kcal/mol)	*ΔG (kcal/mol)*
BTXI-NO$_2$(1)	-35.43	-35.11
BTXI-NO$_2$ (2)	-36.49	-34.89
BTXI-NO$_2$ (3)	-33.16	-31.40
BTXI-NO$_2$ (4)	-44.90	-43.95
BTXI-NO$_2$ (5)	-40.09	-38.96
BTXI-NO$_2$ (6)	-37.31	-35.73
BTXI-NO$_2$ (7)	-40.46	-39.12
BTXI-NO$_2$ (8)	-34.48	-33.79

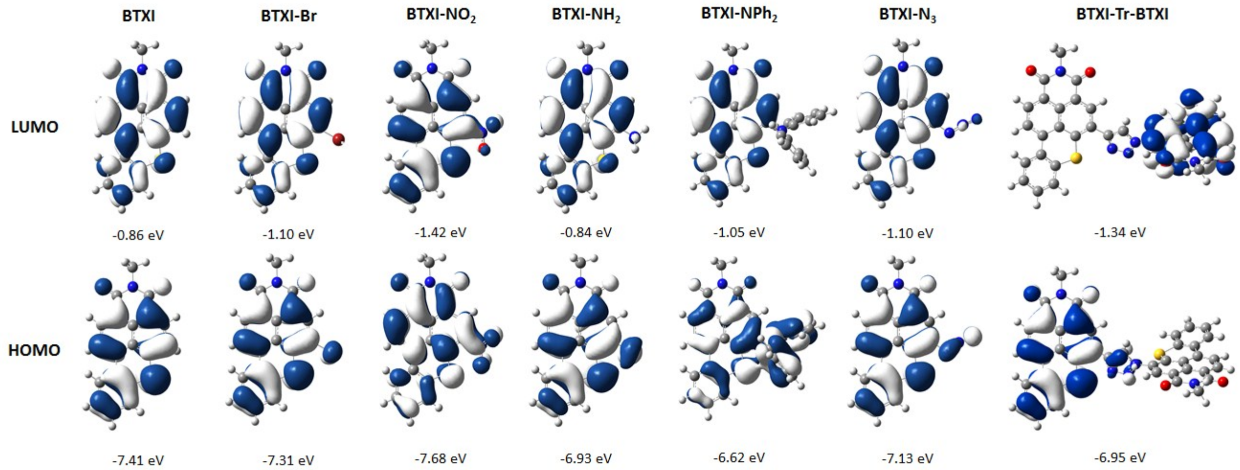

Figure S18. Pictorial representations of select frontier molecular orbitals of **BTXI** derivatives as determined at the OT-ωB97X-D/6-31g(d,p) level of theory.

Table S3. First ten excited states for the **BTXI** derivatives as determined at the TD-OT-ωB97X-D/6-31g(d,p) level of theory

Excited State	BTXI		BTXI-Br		BTXI-NO_2		BTXI-N_3		BTXI-NH_2		BTXI-NPh_2		BTXI-Tr-BTXI	
	Energy [λ] (eV [nm])	***f***	**Energy [λ] (eV [nm])**	***f***	**Energy [λ] (eV [nm])**	***f***	**Energy [λ] (eV [nm])**	***f***	**Energy [λ] (eV [nm])**	***f***	**Energy [λ] (eV [nm])**	***f***	**Energy [λ] (eV [nm])**	***f***
1	3.28 [378]	0.4151	3.25 [382]	0.3974	3.23 [384]	0.3386	3.12 [398]	0.3794	3.06 [405]	0.3116	2.90 [428]	0.1725	3.12 [398]	0.3373
2	4.01 [309]	0.0224	3.91 [317]	0.0116	3.71 [335]	0.1549	3.74 [331]	0.0027	3.77 [329]	0.0134	3.35 [370]	0.1924	3.19 [388]	0.3931
3	4.24 [292]	0.0057	4.15 [299]	0.0093	3.96 [313]	0.0004	3.85 [322]	0.0013	4.04 [307]	0.0682	3.77 [329]	0.0666	3.83 [323]	0.0084
4	4.26 [291]	0.0002	4.22 [294]	0.0002	4.04 [307]	0.0062	4.03 [308]	0.0346	4.24 [292]	0.0002	4.04 [307]	0.1119	3.89 [318]	0.0081
5	4.53 [273]	0.0928	4.49 [276]	0.0799	4.22 [294]	0.0002	4.21 [294]	0.0002	4.53 [274]	0.0686	4.11 [301]	0.0028	3.95 [314]	0.0175
6	4.68 [265]	0.0007	4.64 [267]	0.0098	4.39 [282]	0.0508	4.43 [280]	0.0949	4.58 [270]	0.0681	4.33 [286]	0.0905	4.01 [309]	0.0099
7	4.76 [261]	0.0128	4.67 [266]	0.0468	4.51 [275]	0.0040	4.48 [277]	0.1976	4.67 [266]	0.0007	4.38 [283]	0.0595	4.11 [302]	0.0014
8	5.08 [244]	0.069	4.97 [249]	0.0001	4.61 [269]	0.1574	4.64 [267]	0.0004	5.02 [247]	0.1097	4.56 [272]	0.0769	4.12 [301]	0.0117
9	5.20 [239]	0.0363	5.02 [247]	0.0691	4.64 [267]	0.0019	4.90 [253]	0.2139	5.13 [242]	0.0061	4.56 [272]	0.0195	4.17 [298]	0.0005
10	5.40 [230]	0.0831	5.18 [239]	0.1179	4.84 [256]	0.0220	5.09 [243]	0.1345	5.28 [235]	0.1023	4.65 [267]	0.0157	4.31 [287]	0.0691

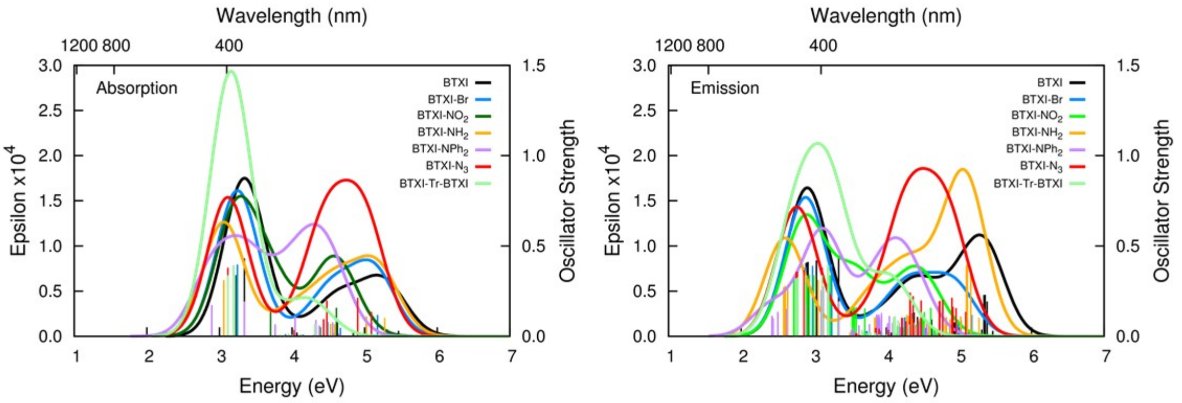

Figure S19. Simulated absorption (left) and emission (right) spectra of **BTXI** derivatives as determined at the OT-ωB97X-D/6-31g(d,p) level of theory. The spectra were simulated through convolution of the vertical transition energies and oscillator strengths with Gaussian functions characterized by a full width at half-maximum (fwhm) of 0.33 eV.

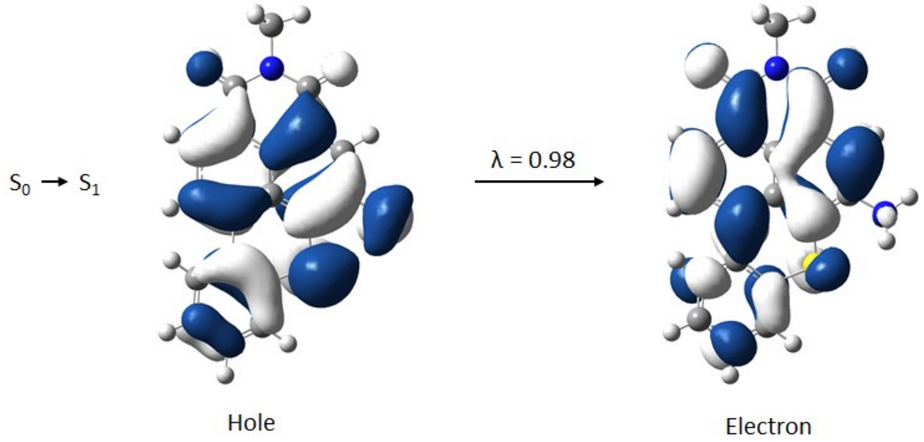

Figure S20. Pictorial representations of the natural transition orbitals (NTO) for the S_0✂S_1 transitions of **BTXI-NH$_2$** as determined at the TD-OT-ωB97X-D/6-31g(d,p) level of theory. λ is the fraction of the hole–particle contribution to the excitation.

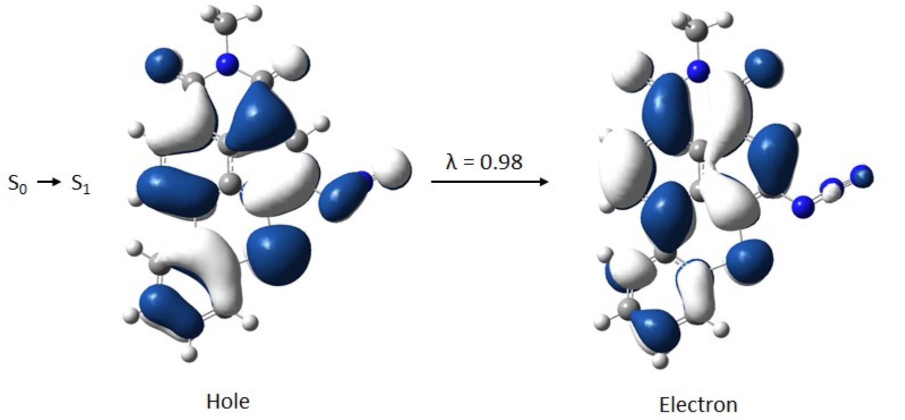

Figure S21. Pictorial representations of the natural transition orbitals (NTO) for the S_0✂S_1 transitions of **BTXI-N$_3$** as determined at the TD-OT-ωB97X-D/6-31g(d,p) level of theory. λ is the fraction of the hole–particle contribution to the excitation.

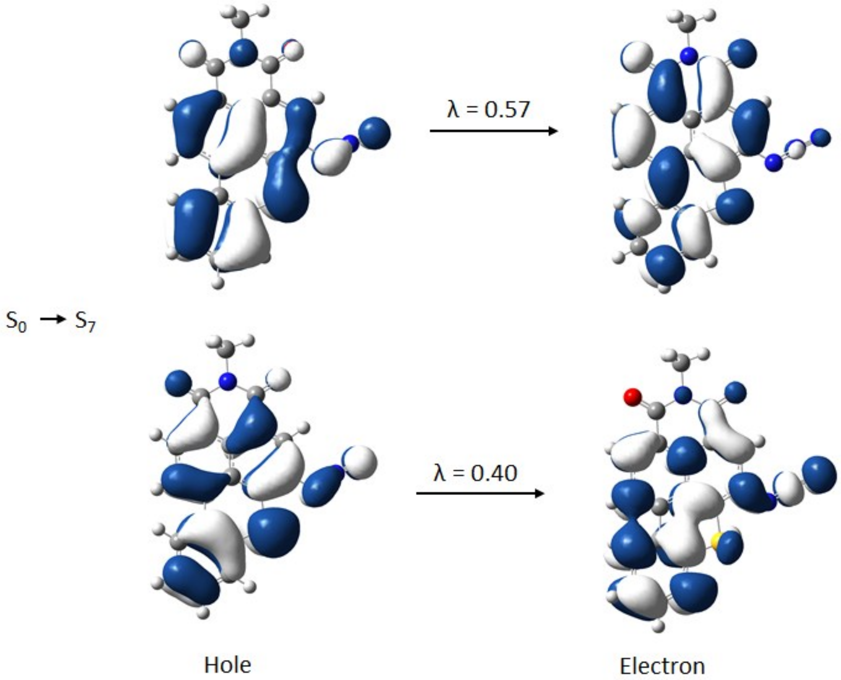

Figure S22. Pictorial representations of the natural transition orbitals (NTO) for the S_0✂S_7 transitions of **BTXI-N_3** as determined at the TD-OT-ωB97X-D/6-31g(d,p) level of theory. λ is the fraction of the hole–particle contribution to the excitation.

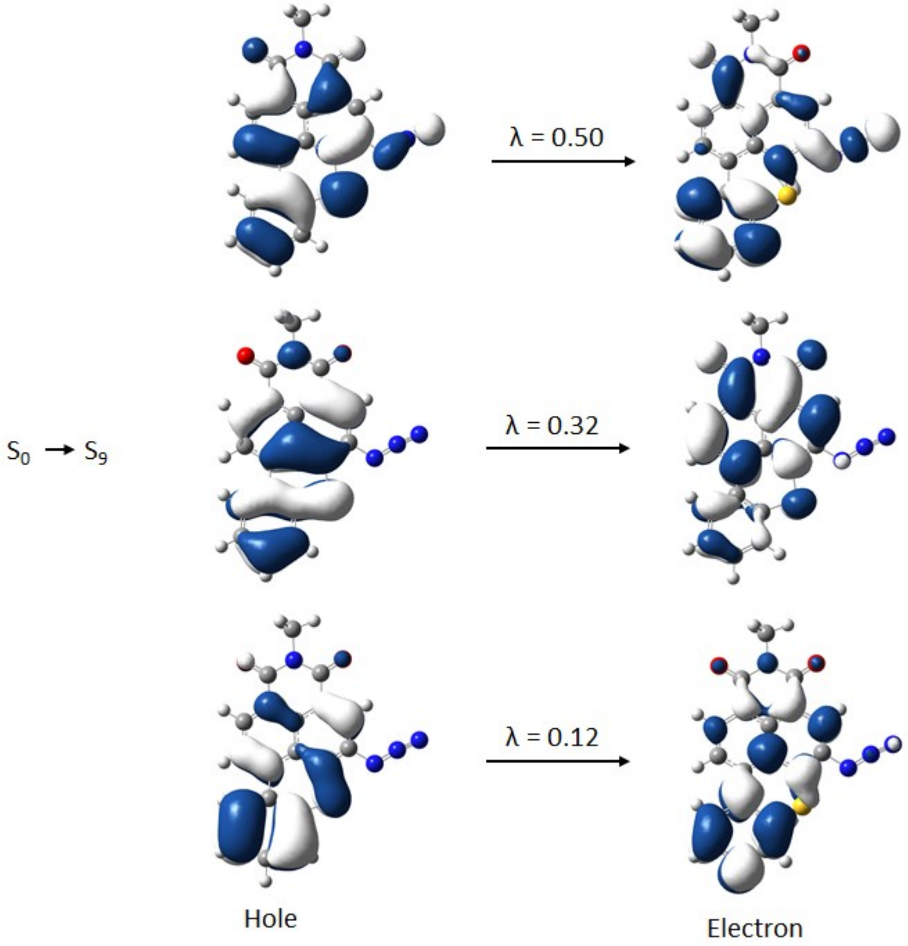

Figure S23. Pictorial representations of the natural transition orbitals (NTO) for the S_0✂S_9 transitions of **BTXI-N_3** as determined at the TD-OT-ωB97X-D/6-31g(d,p) level of theory. λ is the fraction of the hole–particle contribution to the excitation.

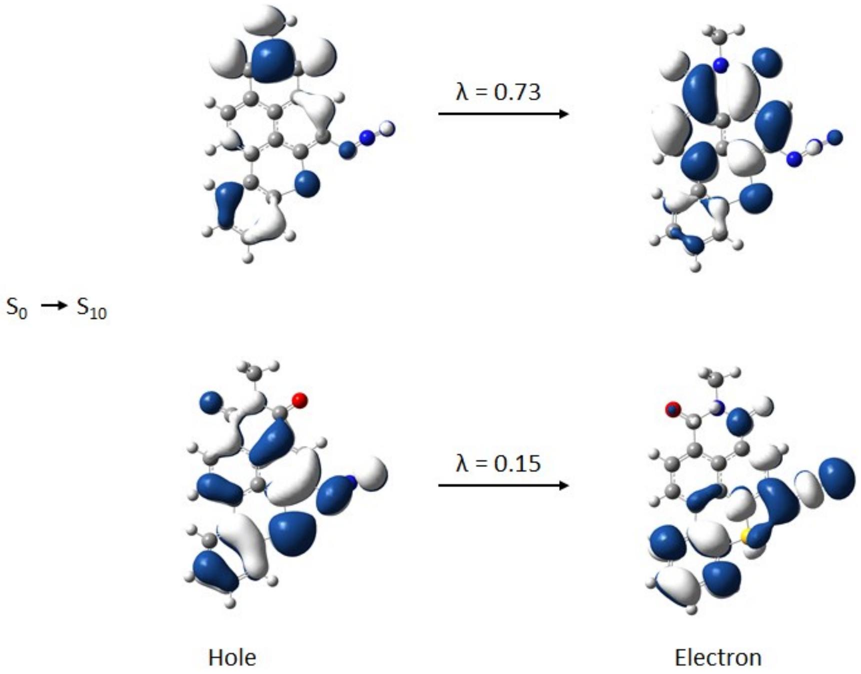

Figure S24. Pictorial representations of the natural transition orbitals (NTO) for the S_0✂S_{10} transitions of **BTXI-N_3** as determined at the TD-OT-ωB97X-D/6-31g(d,p) level of theory. λ is the fraction of the hole–particle contribution to the excitation.

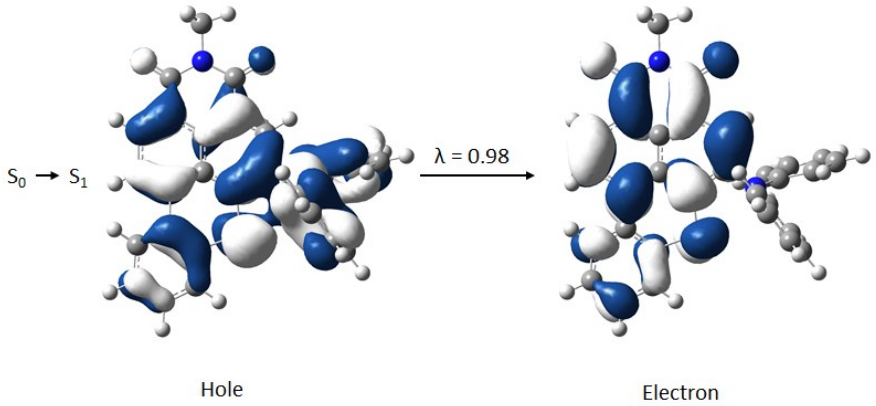

Figure S25. Pictorial representations of the natural transition orbitals (NTO) for the S_0✂S_1 transitions of **BTXI-NPh_2** as determined at the TD-OT-ωB97X-D/6-31g(d,p) level of theory. λ is the fraction of the hole–particle contribution to the excitation.

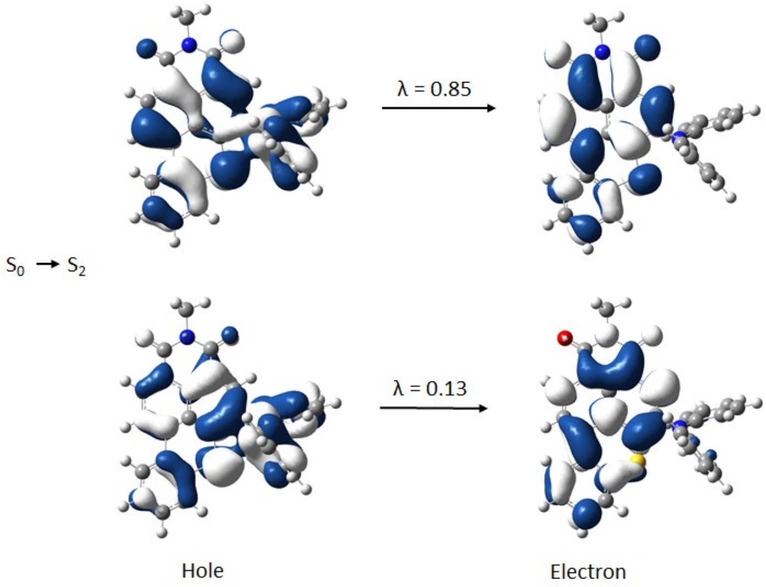

Figure S26. Pictorial representations of the natural transition orbitals (NTO) for the S_0✂S_2 transitions of **BTXI-NPh$_2$** as determined at the TD-OT-ωB97X-D/6-31g(d,p) level of theory. λ is the fraction of the hole–particle contribution to the excitation.

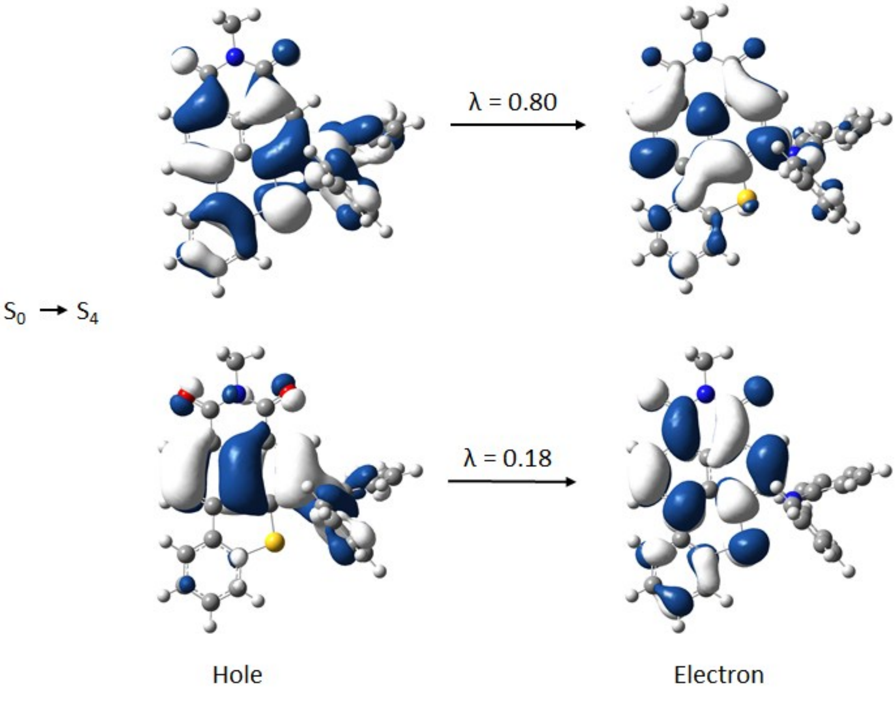

Figure S27. Pictorial representations of the natural transition orbitals (NTO) for the S_0✂S_4 transitions of **BTXI-NPh$_2$** as determined at the TD-OT-ωB97X-D/6-31g(d,p) level of theory. λ is the fraction of the hole–particle contribution to the excitation.

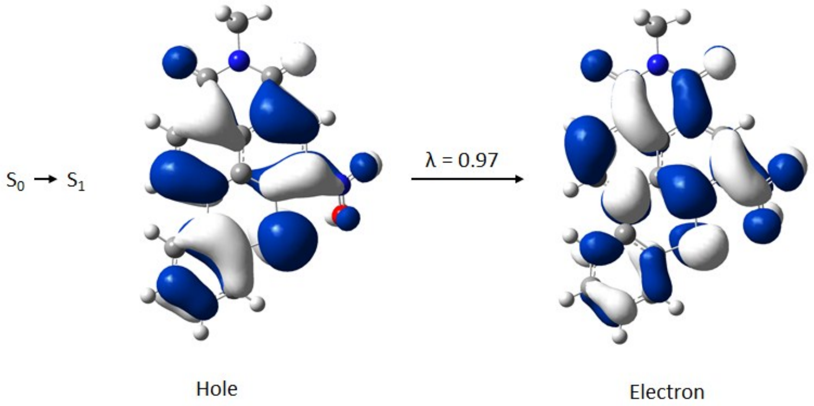

Figure S28. Pictorial representations of the natural transition orbitals (NTO) for the S_0✂S_1 transitions of **BTXI-NO$_2$** as determined at the TD-OT-ωB97X-D/6-31g(d,p) level of theory. λ is the fraction of the hole–particle contribution to the excitation.

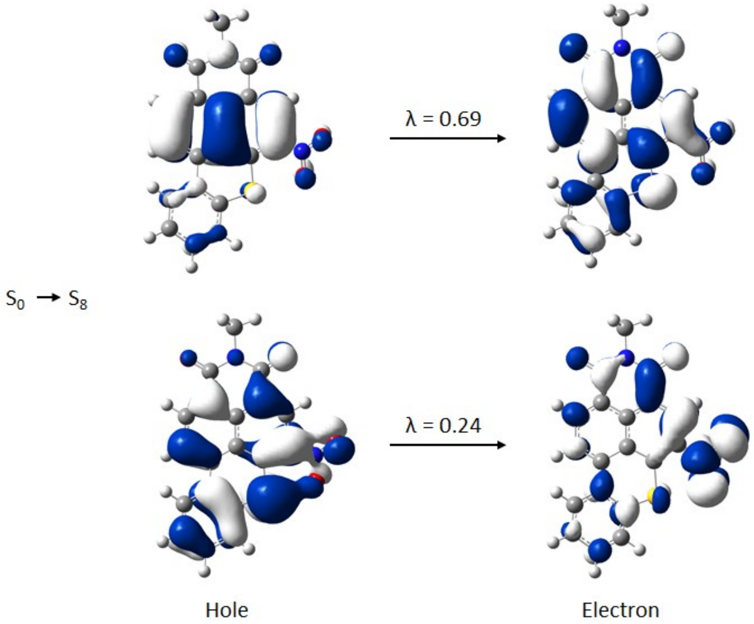

Figure S29. Pictorial representations of the natural transition orbitals (NTO) for the S_0✂S_8 transitions of **BTXI-NO$_2$** as determined at the TD-OT-ωB97X-D/6-31g(d,p) level of theory. λ is the fraction of the hole–particle contribution to the excitation.

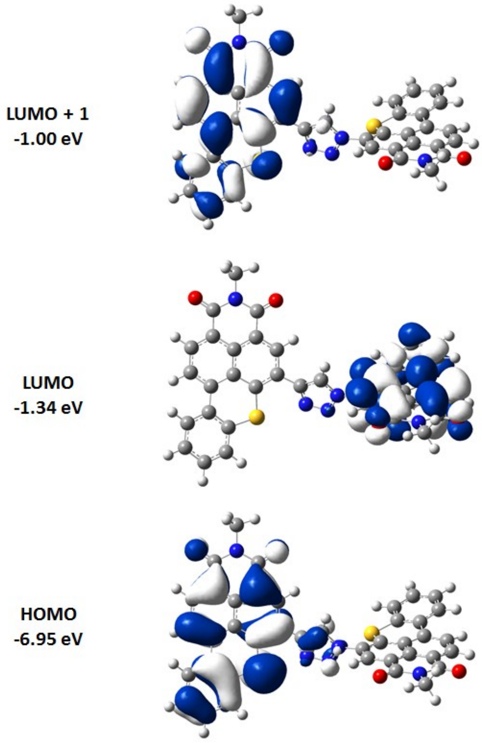

Figure S30. Pictorial representations of select frontier molecular orbitals of **BTXI-Tr-BTXI** as determined at the OT-ωB97X-D/6-31g(d,p) level of theory.

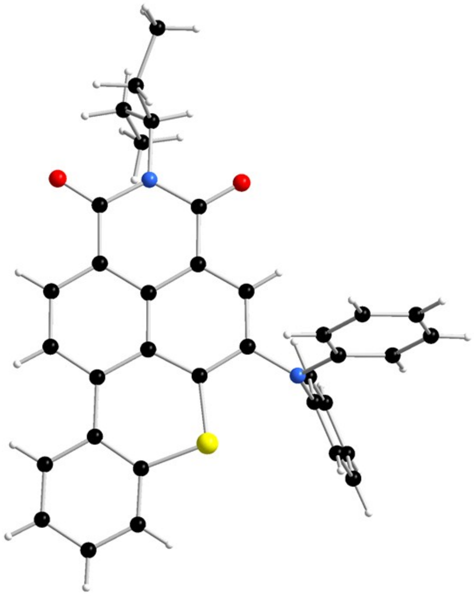

Figure S31. Molecular structure of **BTXI-NPh$_2$** obtained by X-ray diffraction.

Table S4. Crystal Data Collection and Refinement Parameters of **BTXI-NPh$_2$**.

X-ray single-crystal diffraction data were collected on a Rigaku Oxford Diffraction SuperNova diffractometer equipped with Atlas CCD detector and micro-focus Cu-K$_\alpha$ radiation. The structure was solved by direct methods and refined on F^2 by full matrix least-squares techniques using SHELX programs (G. M. Sheldrick, 2018). All non-H atoms were refined anisotropically and multiscan empirical absorption was corrected using CrysAlisPro program (CrysAlisPro, Agilent Technologies, V 1.171.40.45a, 2019). The H atoms were included in the calculation without refinement.

Empirical formula	C_{35} H_{28} N_2 O_2 S
Formula weight	540.65
Temperature (K)	150.0(1)
Wavelength(Å)	1.54184
Crystal system, space group	Orthorhombic, P b c a
a(Å)	17.9272(5)
b(Å)	13.9769(4)
c(Å)	43.7984(8)
α(deg)	90
β(deg)	90
γ(deg)	90
Volume (Å^3)	10974.4(5)
Z	16
Calculated density (g cm^{-3})	1.309
Absorption coefficient (mm^{-1})	1.325
θ range (deg); completeness	4.037 to 72.531; 98.5 %
Data collected / unique / R(int)	26084 / 10497 / 0.0421
Data observed / parameters	7009 / 725
GOF	1.023
R_1 / wR_2 [I > 2σ (I)]	0.0578 / 0.1390
R_1 / wR_2 [all data]	0.0945 / 0.1627
Largest diff. peak and hole	0.753 and -0.341 e.A^-3
CCDC number	1966947